

**1 Reflection of linear internal tides from realistic topography: The
2 Tasman continental slope**

3 JODY M. KLYMAK, *

School of Earth and Ocean Sciences and Department of Physics and Astronomy, University of Victoria, Victoria, Canada

4 Harper L. Simmons and Dmitry Braznikov

University of Alaska Fairbanks, Fairbanks, Alaska, USA

5 Samuel Kelly

Large Lakes Observatory and Department of Physics, University of Minnesota Duluth, Duluth, Minnesota

6 Jennifer A. MacKinnon, Matthew H. Alford, and Robert Pinkel

Scripps Institution of Oceanography, University of California, San Diego, La Jolla, California

7 Jonathan D. Nash

College of Ocean and Atmospheric Science, Oregon State University, Corvallis, Oregon

* Corresponding author address: Jody Klymak, University of Victoria, Victoria, BC, Canada

E-mail: jklymak@uvic.ca

ABSTRACT

9 The reflection of a low-mode internal tide on the Tasman continental slope is investigated
10 using simulations of realistic and simplified topographies. The slope is super-critical to the
11 internal tide, which should predict a large fraction of energy reflected. However, the response
12 to the slope is complicated by a number of factors: the incoming beam is confined laterally;
13 it impacts the slope at an angle; there is a roughly cylindrical rise directly offshore of the
14 slope; and a leaky slope-mode wave is excited. These effects are isolated in simulations
15 that simplify the topography. In order to separate the incident from reflected signal, a
16 response without the reflector is subtracted from the total response to arrive at a reflected
17 signal. The real slope reflects approximately 65% of the mode-1 internal tide as mode-1,
18 less than two-dimensional linear calculations predict, due to the three-dimensional concavity
19 of the topography. It is also less than recent glider estimates, likely due to along-slope
20 inhomogeneity. The inhomogeneity of the response comes from the Tasman Rise which
21 diffracts the incoming tidal beam into two beams, one focused along-beam, and one diffracted
22 to the north. Along-slope inhomogeneity is enhanced by a partially trapped super-inertial
23 slope wave that propagates along the continental slope, locally removing energy from the
24 deep-water internal tide and re-radiating it into the deep water further north. This wave is
25 present even in a simplified straight-slope topography, its character can be predicted from
26 linear resonance theory, and it represents up to 30% of the local energy budget.

²⁷ 1. Introduction

²⁸ Energy is lost from the surface tide when it interacts with topography and, in the deep
²⁹ ocean, is largely redistributed as an internal tide. The fate of the internal tide is unclear, but
³⁰ depends on the dominant wavelengths that are forced. Gentle [The internal tide response to](#)
³¹ topography that is subcritical to the internal tide [frequency](#) is likely dominated by higher
³² vertical modes [and](#) is thought to break via wave-wave interactions relatively close to the
³³ topography (i.e. Polzin 2009; St. Laurent and Garrett 2002). Steeper supercritical topog-
³⁴ raphy, while exhibiting significant local dissipation, tends to radiate a large fraction of the
³⁵ internal tide away from the topography as low-mode waves (i.e. at Hawaii; Klymak et al.
³⁶ 2006; Carter et al. 2008). Given that a significant fraction of the internal tide energy is
³⁷ generated at steep topography (Legg and Klymak 2008), and that the distribution of the
³⁸ mixing it eventually drives has impacts on understanding the distribution of ocean proper-
³⁹ ties and the strength of the overturning circulation (i.e. Melet et al. 2013), it is desirable to
⁴⁰ understand where and how the radiated energy dissipates.

⁴¹ One candidate sink for the low-mode internal tide is scattering and dissipation from
⁴² continental slopes. These slopes are known to be hotspots of turbulent mixing from the few
⁴³ observational studies to date (Nash et al. 2007; Klymak et al. 2011; Martini et al. 2013).
⁴⁴ However, these studies have also demonstrated some of the difficulties in tracking internal tide
⁴⁵ energy on these slopes. Net internal-tide fluxes are relatively straight forward to measure,
⁴⁶ but ideally we would like to separate the incident and reflected fluxes if a parameterization of
⁴⁷ turbulence on the slope is to be made, since the incident fluxes are what drive the turbulence.
⁴⁸ The reflectivity of a continental slope is the ratio of the energy flux convergence divided by

49 the total incident flux:

$$R = \frac{F_{out}}{F_{in}}, \quad (1)$$

50 where F is depth-integrated for a two-dimensional budget or ~~line-integrated~~ depth-line-integrated
51 for a three-dimensional one. Even simple two-dimensional linear models of reflection indicate
52 that determining the reflectivity will be challenging, with reflection co-efficients strongly de-
53 pending on the modal content and phases of the incident internal tides (Klymak et al.
54 2011) and the local surface tide (Kelly and Nash 2010). These linear models have been
55 used globally to estimate reflection co-efficients for the mode-1 tides on realistic continental
56 slope bathymetries, (Kelly et al. 2013b,a), but these calculations assume the incoming tide
57 is known, and that the topography is relatively homogenous over a distance similar to the
58 mode-1 horizontal wavelength.

59 Determining the incident flux, F_{in} , from field data, and even from a numerical model with
60 sufficient complexity, is not trivial. In two dimensions, or with simple ~~plane wave~~ plane-wave
61 geometries, it is straight forward to fit incident and reflected plane waves to recover the
62 desired reflection co-efficient([a](#)). In the real ocean, even if tidal signals can be separated from
63 confounding influences, internal tides are often ~~spatially laterally~~ inhomogeneous, and form
64 lateral “beams” (in x-y; Rainville et al. 2010) that make plane wave fits difficult from a finite
65 array of moorings; for instance a mooring array could be located more in the incoming beam
66 than in the reflected, leading to an exaggeration of the computed energy convergence([b](#)).
67 Plane-wave fits to satellite altimetry tracks are promising, but will also suffer from a lack
68 of fidelity if the internal tides are inhomogeneous on the scale of the plane wave fits (Zhao
69 and Alford 2009). In the model, high resolution temporal and spatial information makes

70 it possible to separate signals spectrally according to their direction of propagation (i.e.
71 using a Hilbert transform, Mercier et al. 2008), but this method works best if there are no
72 boundaries and the signals at the edges of the model domain can be tapered to reduce Gibbs
73 ringing, neither of which are applicable in the nearfield of a continental slope.

74 The region considered here is the Tasman continental slope, the focus of a concentrated
75 internal tide field experiment, [TTIDE](#). As preliminary work, it has been sampled contin-
76 uously by gliders for a number of months in 2012 and 2013 (Johnston et al. 2015). The
77 gliders were ~~fown to form and piloted to form an~~ antenna over which internal plane-wave
78 fits were made. These efforts show a standing wave pattern, with amplitudes and phases as
79 one would expect for internal waves incident on the slope from the southeast where internal
80 tides are expected to be generated from the Macquarie Ridge (figure 1a). The amplitudes
81 of the interfering waves were such that the reflectivity is predicted to be high on this slope,
82 with estimates of 0.7 to 1.0 from the arrays (Johnston et al. 2015). The gliders also picked up
83 a 100-km wavelength wave propagating along slope towards the north, a finding we isolate
84 and discuss below.

85 **Schematic of the difficulty of quantifying reflecting fluxes in an inhomogeneous environment.**
86 ~~Plane waves are trivial. Inhomogeneous incoming waves or reflections are significantly more~~
87 ~~difficult.~~

88 Here we run numerical simulations that are meant to represent a mode-1 internal M_2
89 tide incident on the Tasman Slope, east of Tasmania. The simulations are only forced by the
90 incident internal tide, and there is no ~~local forcing~~ [barotropic forcing anywhere in the domain](#),
91 allowing the reflection signal to be isolated. After discussing the model setup ([section 2](#)),
92 we briefly consider the response this forcing has on the slope ([section 3](#)) and compute and

93 energy budget of the complete response. In order to separate the physics of the reflection,
94 we then simplify the geometry (section 4), both geometrically, and by removing parts of the
95 topography. This technique allows us to separate incident and reflected signals from the
96 total response without appeal to plane wave fits. We end with a discussion of the results
97 (section 5) where we note the applicability of two-dimensional reflection models and discuss
98 the leaky slope waves evident in the simulations. We conclude with a summary (section 6).

99 2. Model setup

100 a. Basics

101 The numerical model used here is the MITGCM (Marshall et al. 1997), visualized using
102 the Python scientific stack (Hunter 2007; van der Walt et al. 2011). The setup is very similar
103 to Buijsman et al. (2014), with the model run in hydrostatic mode, background (isotropic)
104 diffusivities and viscosities of $10^{-5} \text{ m}^2 \text{ s}^{-1}$, and enhanced diffusivity and viscosity in regions
105 of temporarily unstable stratification (Klymak and Legg 2010). A second-order flux-limiting
106 temperature advection scheme is used which results in some numerical dissipation and dif-
107 fusion. Sensitivity tests were run with weaker forcing, and the fraction of energy dissipated
108 in the model did not change, indicating that the dissipation highlighted below is dominated
109 by numerical dissipation due to the lack of lateral resolution (1 km) rather than explicit
110 viscosities. Dissipation is not the main focus of this paper, and finer resolutions have been
111 used for more focused efforts dealing with turbulence on the slope (in preparation). **These**
112 ~~simulations are therefore the most “linear” that the resolution will allow.~~

113 Topography is from a data set that combines Smith and Sandwell (1997) and multibeam
114 data from Australian surveys (Whiteway 2009) (figure 1b). For this paper, we use a Cartesian
115 co-ordinate system centered at 44 S, 148 E, with y pointing 12 degrees east of geographic
116 north (magenta lines, figure 1). This co-ordinate system is close to cross-slope in the x-
117 direction, and is used for conceptual convenience. The simulations are run on a f-plane
118 ($f = -10^{-4} \text{ s}^{-1}$).

119 A 1-km lateral resolution is used along the continental slope (figure 2a, smallest inset
120 green box). Resolution is expanded by 3.5% per grid cell beyond the 1km-resolution region,
121 to a maximum of 5 km in the second largest inset box (figure 2a); this keeps the resolution
122 over the Tasman Rise and the rest of the continental slope at least 5 km. Further out, the
123 grid spacing is again increased at 3.5% per grid cell until a maximum grid cell size of 10 km
124 is reached.

125 Vertical resolution is approximately stretched so $dz \sim 1/N$, where $N^2(z) = -\frac{g}{\rho_0} \frac{d\rho}{dz}$ is the
126 vertical stratification. 200 vertical grid cells are used for these simulations. The vertical
127 stratification is from the World Ocean Atlas for the Tasman Sea just offshore of Tasmania
128 ([Boyer et al. 2013](#))[\(figure 1c Boyer et al. 2013\)](#), and is assumed [to be initially](#) laterally con-
129 stant in the domain. This precludes any mesoscale effects, which are believed to be important
130 in this area, and are the subject of future work.

131 *b. Forcing*

132 To simplify the generation problem we apply an analytical forcing to our model [that](#)
133 [is meant to represent a simplified version of the regional simulation pictured in](#) figure 1a.

134 This is composed of two line sources at approximately the location of the Macquarie Ridge
 135 (figure 2a). The initial conditions ~~and contain this wave field, and sponges in~~ the southern
 136 and eastern boundaries ~~of the model were set with this forcing~~~~are forced with it~~. The forcing
 137 is similar to that suggested by Rainville et al. (2010), except ~~instead of a single point source~~
 138 ~~placed a distance R from the line source, the line source~~ here our line source is digitized as
 139 a number of discrete point sources along the line, and their response in the domain summed.
 140 The mode-1 pressure anomaly is given by:

$$p'(x, y, t) = \sum_{i=1}^N \underbrace{ap'_i}_{\text{a}_i} = \sum_{i=1}^N \frac{a_i}{\sqrt{r_i}} \exp \left(j \left(|\underline{k_t} \underline{\mathbf{k}}| r_i - \omega t \right) \right) \quad (2)$$

141 where a_i is the amplitude of the i-th source, $r_i = \sqrt{(x - x_i)^2 + (y - y_i)^2}$ is the distance to
 142 the source, and $|\underline{k_t} \underline{\mathbf{k}}|$ is the absolute value of the mode-1 wavenumber:

$$\underline{k_t} \underline{|\mathbf{k}|} = \frac{(\omega^2 - f^2)^{1/2}}{c_e} \quad (3)$$

143 where ω is the frequency of the tide, f is the Coriolis frequency, and c_e is the eigenspeed of
 144 the vertical mode equation:

$$\frac{d}{dz} \left(\frac{1}{N^2} \frac{d\psi}{dz} \right) + \frac{1}{c_e^2} \psi(z) = 0. \quad (4)$$

145 Here $\psi(z)$ is the eigenfunction that sets the shape of the vertical mode, and the bound-
 146 ary conditions are $d\psi/dz = 0$ at $z = 0$ and $z = -H$, where H is the water depth. For
 147 convenience, we normalize $\psi_m(z)$ so that

$$\int_{-H}^0 \psi_m(z) \psi_n(z) dz = \delta_{mn}. \quad (5)$$

148 Horizontal velocities can be linearly decomposed by these shapes, as can the pressure signal.

₁₄₉ To compute the wavefield, the horizontal velocity components are derived from the in-
₁₅₀ ternal wave consistency relations:

$$u(x, y, t) = \sum_{i=1}^N \frac{k_x \omega + j k_y f}{\omega^2 - f^2} \frac{p'_i}{\rho} \quad (6)$$

$$v(x, y, t) = \sum_{i=1}^N \frac{k_y \omega - j k_x f}{\omega^2 - f^2} \frac{p'_i}{\rho} \quad (7)$$

₁₅₁ where $k_x = k_t \cos(\theta_i)$ and $k_y = k_t \sin(\theta_i)$ $k_x = |\mathbf{k}| \cos(\theta_i)$ and $k_y = |\mathbf{k}| \sin(\theta_i)$ are calculated
₁₅₂ from the angle to each element of the line sources $\theta_i = \arctan((y - y_i)/(x - x_i))$.

₁₅₃ The resulting incoming wavefield (figure 2a) has a beam of energy flux that radiates
₁₅₄ northwest, and is relatively tightly focused. The interference pattern creates a null to the
₁₅₅ south and north, and a secondary beam that radiates due west. This schematic agrees with
₁₅₆ more realistic regional tidal models (H. Simmons, in preparation), and the amplitude of the
₁₅₇ beam was tuned to give approximately 2 kW m^{-1} incident at Tasmania. Note this is less
₁₅₈ than estimates from altimetry and numerical simulations, and is purposely low to keep the
₁₅₉ runs as “linear” as possible. The initial condition is applied uniformly through the domain,
₁₆₀ regardless of bathymetry, so there are some start-up transients as the proper baroclinic flow
₁₆₁ develops.

₁₆₂ The sponge regions on the southern and eastern boundaries are forced with this forcing.
₁₆₃ The northern and western boundaries are sponges where the velocity is slowly dropped to
₁₆₄ zero and the stratification relaxed to the initial stratification (figure 2a, green rectangles).
₁₆₅ Our main focus is the area from $y=0$ to 400 km, so the boundaries are sufficiently far that
₁₆₆ small residual reflections do not affect the response.

₁₆₇ The ideal response off the Tasman topography would be as a plane-wave reflection from
₁₆₈ a wall at $x = 0$ km (i.e. Johnston et al. 2015). Here we have a relatively confined beam,

169 but we can make a start by considering the reflection the beam from a wall at $x = 0$ km for
170 $y > 0$ km (figure 2b,c) using the method of images with identical line sources mirrored about
171 the y-axis, and their phase shifted by 180 deg. The reflection pattern that sets up is not
172 entirely regular, but has some straight-forward features. The incoming beam impacts the
173 wall at approximately 30 deg. The horizontal wavelength of an M_2 internal tide is 178 km,
174 so the standing wave in the x-direction will have a wavelength $178/\cos(30) \approx 200$ km and
175 in the y-direction will have a wavelength of approximately 350 km. These spatial scales
176 are readily apparent in the analytical forcing despite the non-plane-wave character of the
177 idealized forcing (figure 2c). Note that the standing energy flux (figure 2b) has peaks and
178 nulls in absolute value, with the peaks having large flux to the north. The peaks are every
179 half cross-slope wavelength (i.e. 100 km). The nulls have weak southward energy flux (though
180 it is difficult to discern from the subsampled arrows in the plot).

181 3. Realistic model simulation

182 The response of the forcing in the most real bathymetry motivates the more idealized
183 experiments that follow. From the initial forcing (figure 3a), a complex wavefield develops
184 with clear scattering from the Tasman Rise, the shelf, and numerous small inhomogeneities
185 on the sea floor (figure 3b-d). Looking along slope, the phase of the velocity signal can
186 be seen changing approximately every 200 km, and it changes approximately every 100 km
187 offshelf similar to what we ~~expecte~~ expect from an oblique standing wave (compare figure 3h
188 to figure 2b). However the pattern is complicated, not lining up in the north-south direction
189 and inhomogeneities in the energy that are not accounted for by a simple two-wave model.

190 A time-averaged energy balance is performed online in the model using the terms outlined
191 in Kang and Fringer (2012); Kang (2011). The energy balance vertically integrated can be
192 schematized as:

$$dE_{bc}/dt = -\nabla_H \cdot \mathbf{F}_{bc} + \text{Conversion} - \text{Dissipation}. \quad (8)$$

193 where E_{bc} is the depth-integrated baroclinic energy density, $\mathbf{F}_{bc} \cdot \nabla_H \cdot \mathbf{F}_{bc}$ is the depth
194 integrated ~~energy flux~~baroclinic energy flux convergence, including both the pressure work
195 term and the non-linear advection of energy (which is small in our runs). All quantities
196 are averaged over an M_2 tidal period. “Conversion” is a complex term representing transfer
197 from barotropic motions to baroclinic (Kang 2011, eq. 5.102) and includes the barotropic
198 heaving of the water column, the density anomaly, and a non-linear horizontal advection
199 term. These non-linear terms can be non-trivial in real bathymetry (Buijsman et al. 2014).
200 The conversion term is positive if the barotropic tide loses energy and the baroclinic tide
201 gains energy. “Dissipation” is computed here as the residual, and includes dissipation due
202 to explicit viscosity, numerical dissipation, and bottom drag.

203 Of note in the energy calculation is that the largest local term in the energy budget is an
204 alternating pattern of barotropic-baroclinic conversion at the shelf break, mostly balanced by
205 baroclinic flux convergences and divergences (figure 4). The importance of the barotropic-
206 baroclinic term can also be seen by considering the x-integral of the energy budget from
207 $x = -50$ km to $+100$ km (figure 5). Recall that the simulations have no barotropic forcing.
208 This coupling is ~~catalyzed by~~driven by the interaction of the internal tide and the shelf
209 corner at $y = 0$, and takes the form of a start-up transient hitting the slope with the incoming
210 internal tide beam, and continues throughout the simulation, and is a leaky super-inertial

211 slope wave (see section 5).

212 The time series of the energy terms integrated ~~along the slope~~ in the volume bounded by
213 $x = 0$ to 80 km and $y = 0$ to 400 km demonstrates that the barotropic-to-baroclinic term is
214 relatively small when averaged, with a small loss of energy from the baroclinic tide to the
215 barotropic in the integral region (figure 5b). The model is largely in a steady state by tidal
216 cycle 15, with some residual oscillations in dE/dt and the flux convergence. The oscillations
217 were not explicitly examined, but likely result from imperfect sponges. The large-scale baro-
218 clinic energy changes do not change the dissipation residual very much, which is relatively
219 constant after 5 tidal cycles. To put the 50 MW of dissipation into context, the initial en-
220 ergy that comes in the east and south sides of this analysis box in the initial conditions is
221 315 MW, so the model is dissipating about 17% of the incoming energy. However, note that
222 the dissipation is not the focus of these model runs nor of this paper. The forcing here is
223 approximately a factor 3 lower than the real forcing, so its likely the fraction of dissipation
224 at this site is higher if real forcing is used.

225 The majority of the energy budget is in the first vertical mode (figure 5c). Net fluxes
226 in the region directly offshore of the shelf break ($0 < x < 80$ km, and $0 < y < 400$ km)
227 are composed of substantial mode-1 energy converging on the slope (95 MW net), and some
228 reflected energy escaping in higher modes (28.3 MW, mostly in modes 2–4). The 95 MW net
229 flux is made up of the incoming and reflected mode-1 energy, and separating those terms is
230 the subject of the next section. There is some incoming higher-mode energy as well due to
231 scattering from the Tasman Rise, but as we will also show below, this is minor. The spatial
232 pattern (not shown) of the mode conversion at the continental slope indicates hot-spots for
233 conversion. Modes 2 and 4 have a hotspot of conversion near $y = 250$ km, and mode 3 at

²³⁴ $y = 325$ km.

²³⁵ 4. Simplified geometries

²³⁶ To help tease apart the effects of the Tasman Rise and the non-uniform slope, we carry
²³⁷ out a few simplified experiments (figure 6; figure 7). The REAL case is the one discussed
²³⁸ above (figure 7f). The NO TOPO case has no topography at all (figure 7a), just the beam
²³⁹ being forced at the south and east boundaries and (mostly) absorbed at the west and north.
²⁴⁰ RISE was run with the real bathymetry west of $x = 70$ km (figure 7e). Three idealized ge-
²⁴¹ ometries simplify the physics even more: the SHELF case has a supercritical two-dimensional
²⁴² continental slope running north from $y = 0$ km (figure 7d). ROUND RISE is a 1700-m tall
²⁴³ cylinder-shaped bump with radius of 50 km centered at approximately the same location as
²⁴⁴ the Tasman Rise, with no shelf to the west (figure 7b). The simplified slope and the rise are
²⁴⁵ both used in the SHELF/RISE case (figure 7c).

²⁴⁶ a. *Shelf-only configuration*

²⁴⁷ The simplest topography is the SHELF configuration (figure 7d). Here we have a response
²⁴⁸ that is quite similar to the analytical response calculated above (figure 2b). The only differ-
²⁴⁹ ence between these two cases is the narrow shelf west of $x = 0$ km and the slight slope to
²⁵⁰ the continental slope continental slope instead of a wall. The interference pattern between
²⁵¹ the incoming wave and the reflected wave is clear in this plot, with the same characteristic
²⁵² length scales as above, and a slight bending of the response due to the radial spreading of

253 the beam.

254 The goal of this paper is to determine the amount of reflectivity of the continental slope.

255 This is a hard number to determine in a complicated geometry, and naturally depends on

256 the region of integration. For the SHELF configuration the situation is relatively simple, and

257 we use it to illustrate the numerical technique used below. The signal in the full simulation

258 is assumed to consist of an “incoming” signal and a reflected signal, so we can decompose

259 the east-west velocity amplitude of the first vertical mode (for example) as:

$$u_1^t(x, y) = u_1^i + u_1^r \quad (9)$$

$$v_1^t(x, y) = v_1^i + v_1^r \quad (10)$$

$$p_1^t(x, y) = p_1^i + p_1^r \quad (11)$$

260 where u_1^t is the (total) complex amplitude of the M_2 , mode-1 east-west velocity of the

261 simulation with the reflection, u_1^i of the incoming signal, and u_1^r of the reflected signal. We

262 assume for this example that the incoming signal u_1^i is given by the No TOPO simulation,

263 and u_1^t is from the SHELF simulation. The reflected signal u_1^r is simply the difference of these

264 two. This method has been used by Hall et al. (2013) for a two dimensional flow. Here it is

265 an absolute necessity because of the complicated three-dimensional topography.

266 In order to compute ~~and~~an energy budget, ~~we consider that~~ the energy fluxes are calcu-

267 lated from the decomposed signals as:

$$F_{\underline{u1} \underline{x1}}^t = u_1^t p_1^t \quad (12)$$

$$= \underbrace{u_1^i p_1^i}_{\text{Incoming}} + \underbrace{u_1^r p_1^r}_{\text{Reflected}} + \underbrace{u_1^i p_1^r + u_1^r p_1^i}_{\text{Cross Terms}} \quad (13)$$

$$F_{\underline{v1} \underline{y1}}^t = v_1^t p_1^t \quad (14)$$

$$= \underbrace{v_1^i p_1^i}_{\text{Incoming}} + \underbrace{v_1^r p_1^r}_{\text{Reflected}} + \underbrace{v_1^i p_1^r + v_1^r p_1^i}_{\text{Cross Terms}} \quad (15)$$

268 The cross terms are not negligible for any realistic forcing, and indeed give rise to the
 269 interference patterns seen above (Nash et al. 2004; Martini et al. 2007).

270 The “total” response (figure 8d) consists of the incoming response (figure 8a), and the
 271 “reflected” signal (figure 8b), and substantial cross-terms (figure 8c). The cross terms are
 272 mostly perpendicular to the direction of reflection (i.e. parallel to the slope) and alternately
 273 flux energy to the north and south every half cross-slope wavelength. Combined, these three
 274 components give the “total” flux with net fluxes to the north in alternating peaks every full
 275 offslope wavelength.

276 The reflected response (figure 8b) shows approximately what we would expect with energy
 277 being radiated to the north-east. There is some concentration of this energy at $y \approx 75\text{km}$,
 278 and $y \approx 225\text{km}$ because of coupling with a partially trapped slope wave. This coupling
 279 causes a redistribution of the reflected energy, focusing it approximately every along-slope
 280 wavelength of the slope wave (we show in section 5 that this wavelength changes as the slope
 281 geometry changes).

282 Performing this analysis for the lowest 10 modes, we arrive at an energy budget for the
 283 slope in the green box in the figures ($0 < y < 400 \text{ km}$, and $x < 80 \text{ km}$; figure 8, inset

284 budgets). Note that we assume the flux through $x = 0$ is zero. With this calculation, we see
285 that 408 MW is incident on the slope in mode-1. There is also a net flux of 50 MW into this
286 region from the cross terms. This is a redistribution of energy from north of our box into
287 the box. There is a net convergence of this cross-term energy because there is dissipation in
288 the box; in a purely inviscid solution this term should balance to zero over a closed box. If
289 we extend the integration further north, the cross-term flux drops to zero.

290 Most of the incoming energy reflects back out of the box (figure 8b), with the bulk
291 remaining in mode 1, and some scattering to higher modes. This scattered energy radiates
292 to the north east (not shown). The mode-1 reflection is affected by the slope wave that
293 transfers energy to and from the barotropic tide along the slope, resulting in nulls and peaks
294 in the mode-1 reflection.

295 b. *Tasman Rise ~~only~~ and Simplified Shelf*

296 The Tasman Rise has a profound effect on the energy that impacts the continental slope
297 (figure 7e and f). The incoming beam is almost 500 km wide at $x = 0$ if there is no
298 Tasman Rise, but breaks into three narrower beams when there is a Tasman Rise (figure 7e).
299 Upstream of the rise, the effect is somewhat less energy propagating westward, with an
300 interference pattern towards the east indicating some back reflection.

301 This pattern can be explained in terms of diffraction of the internal tide beam from a
302 deep obstacle (i.e. Johnston and Merrifield 2003). There is a down-wave concentration of
303 energy along the seamount's axis, a null, and sidelobes to the north and south. In this case,
304 the incident beam is of comparable size to the obstacle, leading to an asymmetry, and a

305 stronger lobe to the north than south.

306 Most of the response due to the Tasman Rise can be modeled simply as a cylindrical
307 obstacle in the beam (figure 7b and c). Here our obstacle is 1800 m high in 5000 m of
308 water, and has a radius of 50 km (figure 6). This captures most of the features of the actual
309 Tasman Rise, despite not having a shallow spire in the center and being slightly smaller than
310 the real Rise. The differences make the simplified response have weaker nulls and the whole
311 response is directed a bit further north than the real Rise. Adding the shelf (figure 7c) yields
312 a response that bears substantial similarity to the REAL forcing case.

313 Decomposing into an incoming and reflected signal (figure 9) demonstrates the effect of
314 the Tasman Rise on the response. Less energy is incident on the control volume, largely
315 because the diffraction redirects some of that energy to the north of $y = 400$ km. There is a
316 strong reflection of energy where the main diffraction lobe reflects from the slope (figure 9b),
317 and a smaller maximum just to the north ($y = 250$ km) due to the along-slope wave that
318 is strummed. There is a reflection further north where the northern lobe of the diffraction
319 pattern reflects.

320 The incoming energy has some more high-mode content due to scattering at the cylindri-
321 cal rise (figure 9a), though it is still 95% mode-1. The reflection is almost 80% mode-1, with
322 some scattering to higher modes. The net flux shows approximately 15% of the incoming
323 energy is dissipated at the shelf.

324 c. Real Case

325 The REAL forcing is similar, if more complex (figure 10). The simulation using the
326 bathymetry in the RISE ONLY case (figure 7e) is used as the “Incoming” energy flux, and
327 the REAL (figure 7f) case is the “Total”. Compared to the cylindrical rise, the real Tasman
328 Rise creates a sharper diffraction pattern, and more back reflection. However, the REAL
329 simulation has many of the same features as the SHELF/RISE simulation (figure 7c).

330 Slightly less incoming energy passes into the control volume (figure 10a) because the
331 diffraction by the real Tasman Rise is sharper than the cylindrical rise. As for the cylindrical
332 rise case, there is some incoming higher mode energy due to forward scattering, though again
333 over 95% is mode-1. Reflection is concentrated near $y = 125$ km and $y = 450$ km, associated
334 with the diffraction nodes, with about 85% in mode 1 (figure 10b). Dissipation is less than
335 25% of the incoming energy (figure 10d).

336 5. Discussion

337 a. Estimating reflection co-efficients

338 A major goal of this effort is estimating the fraction of incoming tide that is reflected by
339 the Tasman continental slope to come up with a reflectivity co-efficient. Here we discriminate
340 between the mode-1 reflection, $R_1 = F_{ref,1}/F_{in,1}$, and the total reflection into all the modes,
341 $R_T = F_{ref}/F_{in}$. Evaluating these co-efficients is less straightforward than it may sound
342 because it is difficult to separate the incoming from reflected signal in complicated geometry,
343 even in a fully resolved numerical model, let alone in observations. Above, we used an

344 integrated measure, comparing the incoming flux from a model with no continental slope to
345 one with a continental slope and integrating the fluxes over a control volume from $y = 0$ to
346 400 km. This control volume was an arbitrary choice, but yielded reflectivities of mode -1
347 mode-1 internal tide $R_1 = 0.65$ and the total internal tide of $R_T = 0.76$ (figure 10).

348 The TTIDE field effort deployed a three-point mooring array to quantify the wave field
349 offshore of the continental slope. Determining reflectivity from such a mooring array is sig-
350 nificantly complicated by three-dimensionality and along slope variability. From the mooring
351 array in figure 10, the reflectivity is $R_1 = 0.6/1.3 = 0.46$, a significant under-estimate. The
352 reason for this should be relatively clear from looking at figure 10a,b; the mooring array
353 nicely captures the northward diffracted ray, but catches some of the reflected pattern from
354 the main beam to the south. There are significant interferences in the reflected patterns
355 (figure 10b) because the reflected pattern is a complicated superposition of the cylindrically
356 spreading reflections along the slope.

357 Determining the reflectivity as a function of along-slope direction y is difficult. ~~Simply~~
358 ~~lining up the onslope~~ A simple one-dimensional comparison of onslope and offslope fluxes
359 does not yield useful results because the reflection from any given point on the slope radiates
360 cylindrically, ~~and so~~ it is necessary to integrate over volumes. Here we take the same approach
361 as used in the previous section (i.e. figure 10), but integrate over smaller control volumes
362 (80 km in y , and between 0 and 80 km in x) to see the reflectivity as a function of y
363 (figure 11a,b). The incoming flux every 80 km shows the diffracted beam pattern with a
364 maximum net incoming flux at $y = 120$ km (figure 11a, red line) and a secondary peak to
365 the north at about 440 km. The net reflectivity from these boxes ranges from 0.8 to a low of
366 almost zero at $y = 280$ km where the slope is less steep (figure 11b, solid blue line). Note an

367 uncertainty in the flux decomposition associated with the flux in the cross terms (figure 11a,
368 purple line). This term does not balance to zero, and forms a significant part of the energy
369 budget over such small control volumes. It cannot be uniquely decomposed into either the
370 incoming or reflected energy terms, so remains as an uncertainty.

371 In two-dimensions, the fraction of the tide reflected into mode 1 (and higher) can be
372 predicted from linear theory using the method described by Kelly et al. (2013a) of matching
373 Laplacian tidal solutions at discrete steps on a discretized topography. If the tide is obliquely
374 incident on the slope, there can be substantial differences in the reflected tide (Kelly et al.
375 2013b). If we run these solutions for the Tasman Slope with an incident angle of 30 degrees,
376 the reflectivity into mode-1, R_1 is similar to the numerical simulation (figure 11b, thick black
377 line). The predicted reflectivity is greater for most of the ridge, but the null at $y = 250$ km
378 is captured.

379 The REAL simulation has a mode-1 reflectivity of $R_1 = 0.65$. A naive average of the
380 reflectivity from the linear model between $y = 0$ and 400 km yields $\langle R_1 \rangle = 0.71$. However,
381 that does not take into account the varying strength of the incoming diffracted beam, which
382 is stronger where the reflectivity is higher. Weighting by the incoming beam strength, then
383 the reflectivity averages $\langle R_1 \rangle_{beam} = 0.8$, and is substantially larger than in the numerical
384 simulations.

385 An attempt has been made to estimate reflectivity from this site from autonomous gliders
386 surveys (Johnston et al. 2015). First, the gliders saw a substantial concentration of energy
387 shoreward of the Tasman Rise. This is a feature of the model, and clearly explained by the
388 diffraction of energy by the Tasman Rise (figure 10).

389 For the region in the lee of the Tasman Rise, Johnston et al. (2015) estimate a reflectivity

390 of the mode-1 internal tide of between 0.8 to 1.0 by fitting plane waves to the velocity and
391 displacement amplitudes and phases. If we confine our incoming versus outgoing energy
392 budget to the region $80 \text{ km} < y < 200 \text{ km}$, representative of their *Spray 56* deployment, we
393 calculate a reflectivity of 0.7, which is lower than their lowest estimate of 0.8, and much lower
394 than their high estimate of 1.0. A second deployment, *Spray 55*, covered more of the slope
395 (up to $y = 300 \text{ km}$). In this domain, they estimate a reflectivity of 0.6. This is in agreement
396 with the numerical simulation, which achieves the same result from $0 \text{ km} < y < 300 \text{ km}$.

397 The directions of wave propagation fit from the glider data is not in agreement with the
398 model. The fits to the *Spray 55* data show incoming energy at between 125 and 145 degrees,
399 which is similar to the model. However the reflection is slightly south of due east (0 to
400 -30 degrees geographic), whereas the numerical model is definitely to the northeast far from
401 shore. An explanation is evident from close inspection of figure 10b between the Tasman
402 Rise and the continental slope, where the glider spent the most time. At this location the off-
403 shore energy flux is almost exactly in the x-direction, (-12 degrees geographic), in agreement
404 with the glider observations.

405 Finally, one of the gliders (*Spray 56*) picked out a northward propagating disturbance
406 along the continental slope with wavelength of 100 km. This wavelength matches the wave-
407 length of the slope wave seen in the real simulations (figure 4a,b). Interestingly, they only
408 pick this wavelength out in vertical displacement data, not in velocity.

409 *b. Slope wave importance and dynamics*

410 The structure of the barotropic-to-baroclinic conversion on the slope is an intriguing fea-
411 ture of these simulations, and appears in regional simulations (Simmons, in prep) and the
412 glider data (Johnston et al. 2015). Here, it shows up most clearly in the SHELF simulations
413 because of the simplified bathymetry. However, it is also clear in the REAL simulation (fig-
414 ure 4a). This slope wave redistributes energy in the reflected baroclinic response (figure 8),
415 taking a relatively homogenous incoming energy source and focusing the reflection every 200
416 km or so along slope.

417 This wave is a slope mode that is strummed by the incident internal tide at the “corner” of
418 the topography ($x = 0, y = 0$); a long slope without the corner does not excite this wave, nor
419 does an internal tide coming directly from the east and hitting the topography at a normal
420 angle. The along-slope wavelength is independent of the incident along-slope wavelength
421 in the open water (tested by changing the angle of the incident tide; not shown), and is a
422 robust feature of the slope shape. A sensitivity experiment that varied the continental slope
423 widths demonstrates that narrower slopes strum longer along-slope waves (figure 12).

424 These waves are super-inertial and are an example of partially trapped slope waves (Dale
425 and Sherwin 1996; Dale et al. 2001). We compare the wavelength of the slope waves (fig-
426 ure 13, thick lines) to the empirical modes predicted from linear theory (Dale et al. 2001).
427 The procedure solves for the response of the flow in the coastal bathymetry due to forcing
428 with varying along-slope wavelengths. Resonant along-slope wavelengths lead to a much
429 stronger response (Appendix and figure 13, thin lines). The along-slope wavelength of the
430 resonant modes in the linear calculation agree quite well with the wavelengths of the fully

431 non-linear solutions. Narrower continental slopes yield longer along-slope wavelengths, and
432 the spatial modes that correspond to the peaks are similar to deep-ocean mode-1 off the
433 slope.

434 The slope wave is an important term in the local energy budget when compared the
435 incoming and reflected energy fluxes (figure 14). The incoming energy peaks at 1.2 kW/m,
436 and the reflected energy is of a similar magnitude but with oscillations at twice the wave-
437 length of the slope wave. The integrated barotropic-baroclinic conversion is as high as 0.4
438 kW/m-coastline, and leads to 0.4 kW/m peak-to-peak oscillation in the reflected energy (its
439 not 0.8 kW/m peak-to-peak because the reflected energy spreads spherically by ~~40~~ $x = 40$
440 km, where the reflected flux is evaluated, figure 8). This turns even a relatively straight slope
441 into a series of internal tide absorbers and radiators, leading to 100-km scale inhomogeneity
442 in the reflected internal tide.

443 6. Summary

444 A mode-1 internal tide was launched at a variety of topographies representing the Tasmanian
445 continental slope. The goal was to determine the “reflectivity” of this slope, in terms of
446 the modal content of the reflected energy and the local dissipation. The latter is somewhat
447 suspect in this model because of crude lateral resolution, but the REAL simulation indicated
448 that 21% of the incoming energy was dissipated, and 65% was reflected as mode-1 energy.
449 The incoming internal tide flux used here was weak compared to the flux modeled and in-
450 ferred from altimetry in the Tasman Sea, so we expect the dissipation in more realistically
451 forced models to increase.

452 Despite a simple incoming internal tide that is linear, semi-diurnal, and mode-1, we have

453 found a rich and complex response ~~of the topography~~ when the remote wave impacts the

454 topography. The response can be characterized as follows:

455 • diffraction of the beam by the Tasman Rise,

456 • oblique reflection from the continental slope,

457 • and a leaky slope wave response that redistributes reflected internal energy along-slope.

458 Of these, perhaps only the second effect was expected before carrying out the simulations.

459 However, as we saw above, even the reflection problem is significantly complicated in the

460 presence of three-dimensionality.

461 Diffraction around underwater topography should have been expected, however, the rel-

462 ative depth of the ~~obstaele~~ [Tasman Rise](#) makes it surprising that the effect is so strong. The

463 fact that the lateral width of the ~~Tasman~~-Rise is close to the wavelength of the incoming

464 internal tide makes predicting the diffraction pattern difficult. Baines (2007) considers gen-

465 eration of internal tides at seamounts, but does not deal with scattering and diffraction. The

466 problem is similar to electromagnetic waves passing through a wire, but a linear response

467 for that problem is not trivial to compute (i.e. Bonod et al. 2005), and ~~still~~-does not have a

468 confined vertical mode structure as we find in the internal wave problem.

469 The excitation of slope waves has been explored by Dale et al. (2001). It has an important

470 effect on the redistribution of energy along slope. The redistribution affects where high

471 dissipation is found in the model (figure 4), and adds more inhomogeneity to the reflected

472 internal tide.

473 The complexity grows if other real-world influences are to be accounted for. The East
474 Australian Current flows along this slope, varying the stratification in the horizontal, provides
475 lateral shears that can distort the internal tide response, and carrying eddies that can add
476 a strong time dependence to these effects. Even in two dimensions, the strength of the
477 internal tide reflection can be significantly impacted by the phase of the incoming tide with
478 other baroclinic modes Klymak et al. (2011) or the barotropic (Kelly and Nash 2010). The
479 simulations here exclude the local barotropic tide, so this would certainly complicate the
480 reflected response. Finally, the internal tide used here was monotonic, whereas the real tide
481 will also have other frequencies, most notably subinertial diurnal frequencies that will have
482 trapped wave responses (personal communication, R. Musgrave).

483 Regardless, it is useful to have studied the “simplest” response we could in this system
484 to tease apart the dominant physics. This response is complex, and it should be clear that
485 solely observational efforts to balance a reflection budget are going to be a challenge. Merging
486 simulations and observations is a likely way forward in understanding the wave field in this
487 complex slope region.

488 With respect to the reflection problem, the modeled slope has a relatively high reflection
489 back into the open ocean, with as much as 65% of the incoming energy being reflected as
490 mode-1. Its possible that higher resolution runs will be more dissipative, and that stronger
491 forcing will lead to a higher fraction of dissipation. However, these simulations, and the
492 results from the rest of the experiment to date (i.e. Johnston et al. 2015) indicate that bulk
493 of the energy from the Macquarie Ridge must dissipate elsewhere.

494 *Acknowledgments.*

495 Our thanks to conversations with Andy Dale on leaky slope waves and Qiang Li for
496 sharing his linear code for the Lindzen-Kuo method. J. Klymak was supported by the
497 Canadian National Science Engineering Research Council Discovery Grant 327920-2006, and
498 by computer time from the US Office of Naval Research, T. Palusziewicz, program officer.
499 H. Simmons and D. Brazhnikov were supported by NSF OCE 1130048. J. MacKinnon, and
500 R. Pinkel were supported by award NSF OCE 1129763. M. Alford was supported by NSF
501 OCE 1129246. A website for this paper with analysis scripts, intermediate data files, and
502 model setups is at <http://web.uvic.ca/~jklymak/ttide15>.

APPENDIX

Appendix Slope-wave calculation

506 The slope wave calculation follows the calculation made by Dale et al. (2001), where
 507 there are more details. The linear equation for the pressure perturbations are assumed to
 508 have form $P = p(x, z) \exp^{i(k_y y - \omega t)}$, where k_y is the along-slope wavenumber.

$$(f^2 - \omega^2) \frac{\partial}{\partial z} \left(\frac{\partial p / \partial z}{N^2 - \omega^2} \right) + \frac{\partial^2 p}{\partial x^2} - k_y^2 p = 0 \quad (\text{A1})$$

509 Subject to boundary conditions at the surface of $\partial p / \partial z = 0$ and at the sea floor of

$$\left(\frac{\omega^2 - f^2}{N^2 - \omega^2} \right) \frac{\partial p}{\partial z} = \frac{\partial h}{\partial x} \left(\frac{\partial p}{\partial x} - \frac{f k_y}{\omega} p \right) \quad (\text{A2})$$

510 The coast is assumed to be a wall, and the open ocean to consist of waves radiating away
 511 from the slope, or if k_x , the cross-slope wavenumber, is imaginary, disturbances that decay
 512 away from the slope.

513 The above are discretized on a domain that is 260 km wide into 261 grid cells in x ,
 514 and onto a sigma-co-ordinate with 192 vertical levels. The hyperbolic method of solution
 515 due to Lindzen and Kuo (1969) was used to solve on this domain for p for $\omega = 1.4f$,
 516 $f = 10^{-4} \text{s}^{-1}$, and for a sweep of k_y . Under an arbitrary forcing certain values of k_y resonate
 517 and lead to stronger amplitude responses in p corresponding to spatial modes of the system.
 518 The numerical method is sensitive to the stratification, so we used a fit exponential of
 519 $N^2(z) = 2 \times 10^{-5} \text{s}^{-2} e^{z/(1000 \text{ m})}$ (where z is negative downwards). The scan was taken over
 520 300 wavelengths equally spaced between 30 and 180 km.

521 The resulting spatial modes are similar to those in Dale et al. (2001) (figure 15). There
522 is a peak of amplitude on the shelf, and then a second peak on the slope. As the slope gets
523 more narrow, the peak on the slope becomes broader. These shapes are the lowest modes.

524 The general code to solve this is at <https://github.com/jklymak/LindzenKuo>. The
525 code used for this paper is at <http://web.uvic.ca/~jklymak/ttide15/>.

REFERENCES

- 528 Baines, P. G., 2007: Internal tide generation by seamounts. *Deep Sea Res. I*, **54** (9), 1486 –
 529 1508, doi:10.1016/j.dsr.2007.05.009.
- 530 Bonod, N., E. Popov, and M. Nevière, 2005: Differential theory of diffraction by finite
 531 cylindrical objects. *JOSA A*, **22** (3), 481–490, doi:10.1364/JOSAA.22.000481.
- 532 Boyer, T., et al., 2013: *World Ocean Database 2013*. NOAA Atlas NESDIS 72, doi:10.7289/
 533 V5NZ85MT.
- 534 Buijsman, M. C., et al., 2014: Three-dimensional double-ridge internal tide resonance in
 535 Luzon Strait. *J. Phys. Oceanogr.*, **44** (3), 850–869, doi:10.1175/JPO-D-13-024.1.
- 536 Carter, G., et al., 2008: Energetics of M 2 Barotropic-to-Baroclinic Tidal Conversion at the
 537 Hawaiian Islands. *Journal of Physical Oceanography*, **38** (10), 2205–2223, doi:10.1175/
 538 2008JPO3860.1.
- 539 Dale, A. C., J. M. Huthnance, and T. J. Sherwin, 2001: Coastal-trapped waves and
 540 tides at near-inertial frequencies. *J. Phys. Oceanogr.*, **31** (10), 2958–2970, doi:10.1175/
 541 1520-0485(2001)031<2958:CTWATA>2.0.CO;2.
- 542 Dale, A. C. and T. J. Sherwin, 1996: The extension of baroclinic coastal-trapped wave
 543 theory to superinertial frequencies. *J. Phys. Oceanogr.*, **26** (11), 2305–2315, doi:10.1175/
 544 1520-0485(1996)026<2305:TEOBCT>2.0.CO;2.

- 545 Hall, R. A., J. M. Huthnance, and R. G. Williams, 2013: Internal wave reflection on shelf
546 slopes with depth-varying stratification. *J. Phys. Oceanogr.*, **43** (2), 248–258, doi:10.1175/
547 JPO-D-11-0192.1.
- 548 Hunter, J. D., 2007: Matplotlib: A 2D graphics environment. *Comput. Sci. Eng.*, **9** (3),
549 90–95, doi:10.1109/MCSE.2007.55.
- 550 Johnston, T. M. S., D. L. Rudnick, and S. M. Kelly, 2015: Standing internal tides in the Tas-
551 man Sea observed by gliders. *J. Phys. Oceanogr.*, **45** (11), doi:10.1175/JPO-D-15-0038.1.
- 552 Johnston, T. S. and M. A. Merrifield, 2003: Internal tide scattering at seamounts, ridges,
553 and islands. *J. Geophys. Res.*, **108** (C6), 3180, doi:10.1029/2002JC01528.
- 554 Kang, D., 2011: Barotropic and baroclinic tidal energy. Ph.D. thesis, Stanford University.
- 555 Kang, D. and O. Fringer, 2012: Energetics of barotropic and baroclinic tides in the Monterey
556 Bay area. *J. Phys. Oceanogr.*, **42** (2), 272–290, doi:10.1175/JPO-D-11-039.1.
- 557 Kelly, S. and J. Nash, 2010: Internal-tide generation and destruction by shoaling internal
558 tides. *Geophys. Res. Lett.*, **37**, L23 611, doi:10.1029/2010GL045598.
- 559 Kelly, S. M., N. L. Jones, and J. D. Nash, 2013a: A coupled model for Laplace's tidal
560 equations in a fluid with one horizontal dimension and variable depth. *J. Phys. Oceanogr.*,
561 doi:10.1175/JPO-D-12-0147.1.
- 562 Kelly, S. M., N. L. Jones, J. D. Nash, and A. F. Waterhouse, 2013b: The geography of
563 semidiurnal mode-1 internal-tide energy loss. *Geophys. Res. Lett.*, doi:10.1002/grl.50872.

- 564 Klymak, J., M. Alford, R. Pinkel, R. Lien, Y. Yang, and T. Tang, 2011: The breaking and
565 scattering of the internal tide on a continental slope. *J. Phys. Oceanogr.*, **41**, 926–945,
566 doi:10.1175/2010JPO4500.1.
- 567 Klymak, J. M. and S. M. Legg, 2010: A simple mixing scheme for models that resolve
568 breaking internal waves. *Ocean Modell.*, **33** (3-4), 224 – 234, doi:10.1016/j.ocemod.2010.
569 02.005.
- 570 Klymak, J. M., et al., 2006: An estimate of tidal energy lost to turbulence at the Hawaiian
571 Ridge. *J. Phys. Oceanogr.*, **36**, 1148–1164, doi:10.1175/JPO2885.1.
- 572 Legg, S. and J. M. Klymak, 2008: Internal hydraulic jumps and overturning generated by
573 tidal flow over a tall steep ridge. *J. Phys. Oceanogr.*, **38** (9), 1949–1964, doi:10.1175/
574 2008JPO3777.1.
- 575 Lindzen, R. and H.-L. Kuo, 1969: A reliable method for the numerical integration of a large
576 class of ordinary and partial differential equations. *Mon. Wea. Rev.*, **97** (10), 732–734,
577 doi:10.1175/1520-0493(1969)097<0732:ARMFTN>2.3.CO;2.
- 578 Marshall, J., A. Adcroft, C. Hill, L. Perelman, and C. Heisey, 1997: A finite-volume, incom-
579 pressible Navier-Stokes model for studies of the ocean on parallel computers. *J. Geophys.
580 Res.*, **102** (C3), 5753–5766, doi:10.1029/96JC02775.
- 581 Martini, K., M. Alford, J. Nash, E. Kunze, and M. Merrifield, 2007: Diagnosing a partly
582 standing internal wave in Mamala Bay, Oahu. *Geophys. Res. Lett.*, **34** (17), L17604,
583 doi:10.1029/2007GL029749.

- 584 Martini, K. I., M. H. Alford, E. Kunze, S. M. Kelly, and J. D. Nash, 2013: Internal bores and
585 breaking internal tides on the Oregon continental slope. *J. Phys. Oceanogr.*, **43**, 120–139,
586 doi:10.1175/JPO-D-12-030.1.
- 587 Melet, A., R. Hallberg, S. Legg, and K. Polzin, 2013: Sensitivity of the ocean state to the
588 vertical distribution of internal-tide-driven mixing. *J. Phys. Oceanogr.*, **43** (3), 602–615,
589 doi:10.1175/JPO-D-12-055.1.
- 590 Mercier, M. J., N. B. Garnier, and T. Dauxois, 2008: Reflection and diffraction of internal
591 waves analyzed with the Hilbert transform. *Phys. Fluids*, **20** (8), 086 601, doi:10.1063/1.
592 2963136.
- 593 Nash, J., M. Alford, E. Kunze, K. Martini, and S. Kelley, 2007: Hotspots of deep
594 ocean mixing on the Oregon continental slope. *Geophys. Res. Lett.*, **34**, L01 605,
595 doi:10.1029/2006GL028 170.
- 596 Nash, J. D., E. Kunze, J. M. Toole, and R. W. Schmitt, 2004: Internal tide reflection and
597 turbulent mixing on the Continental Slope. *J. Phys. Oceanogr.*, 1117–1134, doi:10.1175/
598 1520-0485(2004)034<1117:ITRATM>2.0.CO;2.
- 599 Polzin, K. L., 2009: An abyssal recipe. *Ocean Modelling*, **30** (4), 298–309, doi:10.1016/j.
600 ocemod.2009.07.007.
- 601 Rainville, L., T. Johnston, G. S. Carter, M. A. Merrifield, R. Pinkel, P. F. Worcester, and
602 B. D. Dushaw, 2010: Interference pattern and propagation of the M_2 internal tide south
603 of the Hawaiian Ridge. *J. Phys. Oceanogr.*, **40** (2), doi:10.1175/2009JPO4256.1.

- 604 Smith, W. and D. Sandwell, 1997: Global sea floor topography from satellite altimetry and
605 ship depth soundings. *Science*, **277** (5334), 1956, doi:10.1126/science.277.5334.1956.
- 606 St. Laurent, L. and C. Garrett, 2002: The role of internal tides in mixing the deep ocean. *J.*
607 *Phys. Oceanogr.*, **32**, 2882–2899, doi:10.1175/1520-0485(2002)032<2882:TROITI>2.0.CO;
608 2.
- 609 van der Walt, S., S. C. Colbert, and G. Varoquaux, 2011: The NumPy array: A structure
610 for efficient numerical computation. *Comput. Sci. Eng.*, **13** (2), 22–30, doi:10.1109/mcse.
611 2011.37.
- 612 Whiteway, T., 2009: Australian bathymetry and topography grid, june 2009. scale 1:5000000.
613 Tech. rep., Geoscience Australia, Canberra. doi:10.4225/25/53D99B6581B9A.
- 614 Zhao, Z. and M. H. Alford, 2009: New altimetric estimates of mode-1 M2 internal tides
615 in the central North Pacific Ocean. *J. Phys. Oceanogr.*, **39** (7), 1669–1684, doi:10.1175/
616 2009JPO3922.1.

617 List of Figures

618 1 Location of ~~TTide experiment~~TTIDE field site: a) Energy flux in a regional
619 numerical simulation. Color is the absolute value of the flux, arrows it's direc-
620 tion. The magenta box indicates the numerical modeling domain used in this
621 paper. b) Detail of the bathymetry on the Tasman slope. The magenta lines
622 indicate 100 km in the x-direction, and 300 km in the y direction in the mod-
623 eling domain used in this paper. c) The stratification used for all runs in this
624 paper, taken from the World Ocean Atlas at 152 E, 44 S (Boyer et al. 2013).
625 The steps are due to linear interpolation of the density between the atlas
626 depths.

39

627 2 a) ~~Forcing~~ Energy flux representation of the analytical response to the forcing
628 used to drive the models used in this paper. Two mode-1 internal wave
629 sources are located to the south east (blue lines). The model domain is rotated
630 12 degrees from geographic so the shelf break approximately lies along $x =$
631 0. ~~Typical~~ The outer model domain ~~is the rectangle with the thick green~~
632 ~~line. The inner green rectangle denotes 1-km lateral resolution. Outside~~
633 ~~this rectangle resolution increases 3.5% per cell to a maximum of 5-km in~~
634 ~~the second largest rectangle, and outside this rectangle grid size increases to a~~
635 ~~maximum of 10 km. The sponge region-layer is indicated as green rectangles by~~
636 ~~the largest thin-green rectangle.~~ The 250, and 3000-m isobaths are contoured,
637 ~~though the bathymetry is not used in the analytical response.~~ Arrows show
638 the direction of the energy flux, and are scaled by its strength. b) Energy
639 flux of analytical response of energy reflecting from a wall at $x = 0$, north of
640 $y = 0$, ~~in a flat-ocean domain.~~ c) Phase of reflected response.

40

641 3 a)–d) Surface x-direction velocity for four snapshots. a) is the initial condi-
642 tions (slightly modified after a tidal cycle) and d) is the steady state. Grey
643 contours are depths at 3000, 2000, 1000, and 250-m. e)–h) is depth-integrated
644 baroclinic energy flux at the same time periods, with arrows indicating direc-
645 tion.

41

646 4 Energy budget over the 19th tidal cycle of a) Barotropic to baroclinic con-
647 version; b) Baroclinic energy flux convergence ($-\nabla F_{bc}$); c) rate of change
648 of baroclinic energy; d) residual representing the dissipation in the model
649 $D = -\nabla \mathbf{F}_{bc} + \text{Conv.} - dE/dt$. The green box is the region for the energy time
650 series (figure 5b). 42

651 5 a) Integral in x to 80 km offshore of the energy terms in figure 4 for the REAL
652 case (averaged over 20th tidal cycle). Note that the barotropic-baroclinic
653 term (red) is of the same order as the baroclinic convergence (cyanblue)
654 and the residual dissipation (gray) for most of the slope. b) Energy bud-
655 get time series for the “Real” case, tidally averaged, where time is normalized
656 by $T = 12.4$ h, between $y = 0$ to $y = 400$ km. There is still a small
657 residual increase in the energy with time (purple), representing the accumu-
658 lation of high-mode energy in the region. Net barotropic-baroclinic conversion
659 (red) is small and negative, indicating a small net loss to the barotropic tide
660 in this region. The bulk of the budget is the balance between baroclinic
661 flux convergence (blue) and the residual “dissipation” (gray). c) Net flux
662 (averaged over 20th tidal cycle) in the box defined by $0 < x < 80$ km, and
663 $0 < y < 400$ km. Green is the value for the net flux (no modal decomposi-
664 tion). Blue bars are the modal decomposition. There is a net incoming flux
665 in mode 1 and net reflecting fluxes in higher modes (primarily modes 2-4). 43

666 6 Cross sections of topographies from $y = 50$ km. 44

- 667 7 Energy flux for six geometries at tidal cycle 20. Grey depth contours are
 668 -3000, -2000, -1000 and -250 m. Arrows indicate the direction of energy flux.
 669 See figure 6 for bathymetry cross sections at $y = 50$ km. 45
- 670 8 Mode-1 decomposition of energy fluxes averaged for the 20th tidal cycle for the
 671 SHELF experiment. a) Incoming energy flux calculated from the NO TOPO
 672 simulation (figure 7a). Note that the shelf bathymetry is contoured on this
 673 plot (grey lines, and green “land”), but this bathymetry was not part of this
 674 simulation. The green line demarks the region the energy budget in the inset
 675 was integrated over. The green diamonds are the location of a synthetic
 676 mooring, and the arrow indicates the estimated incoming flux from a plane
 677 wave fit over the three moorings of the “Total” simulation (see text). b)
 678 Reflected energy flux calculated from the difference between the velocities and
 679 displacements of the Total simulation (panel d) and the “Incoming” (panel a).
 680 Blue arrow is the outgoing flux from a plane wave fit over the mooring array
 681 from the “Total” simulation. c) Energy flux cross terms between the incoming
 682 and outgoing waves. d) Total simulation from the SHELF case (figure 7d) 46
- 683 9 Energy partition as in figure 8, taking the ROUND RISE simulation as the
 684 incoming wave, and SHELF/RISE simulation as the total wavefield. 47
- 685 10 Energy partition as in figure 8, taking the RISE simulation as the incoming
 686 wave, and REAL simulation as the total wavefield. 48

687 11 a) Energy budget from 80 km by 80 km control volumes along the continental
688 slope from the 20th tidal cycle of the REAL simulations. The incoming flux
689 (red) is compared to the reflected (blue) and the cross terms (purple). b)
690 The reflection co-efficients. The blue line is R_1 , the mode-1 reflectivity in the
691 80-km control volumes along slope from the non-linear simulation. The black
692 line is the mode-1 reflectivity from a linear model (Kelly et al. 2013a), and
693 the next four grey lines ~~behind~~ are the cumulative sum of modes 2 ~~, to 5,~~ and
694 ~~then the last grey line the sum of~~ all the ~~modes~~ reflected energy. These do not
695 sum up to one because the linear model has some “viscosity” that removes
696 some high-mode energy. The dashed lines are the mean of R_1 from the linear
697 model if a constant average is taken (light blue, dashed), and if weighted by
698 the diffracted beam strength (purple, dashed).

49

699 12 Barotropic to baroclinic conversion averaged over the 18-th tidal period for
700 different shelf widths ~~from widest (a) to narrowest (100 km, b) 70 km, c) 40~~
701 km, and d) 20 km. Arrows are barotropic flux vectors. Note how the along-
702 slope barotropic flux is almost entirely confined to conversion dipoles along
703 slope.

50

704 13 Along-slope spectra of across slope velocity (thick lines) for the three narrow-
705 est slopes in figure 12, from velocities on the shallow shelf in these simulations.
706 The thin lines are resonance curves, formed from the cross-slope equations of
707 motion assuming harmonic motion in time and along-slope. As along-slope
708 wavenumber is varied resonant modes have a stronger response. What is
709 plotted is arbitrary units for the three slope geometries.

51

- 710 14 Terms from the energy budget for 40-km wide slope. The incoming and re-
flected energy fluxes are computed at $x = 40$ km, and the conversion term
integrated from the shelf to $x = 40$ km. 52
- 711
- 712
- 713 15 Spatial shape of modes picked out from the resonant searching technique (as
shown in figure 13) for the 70, 40 and 20-km wide slopes. 53
- 714

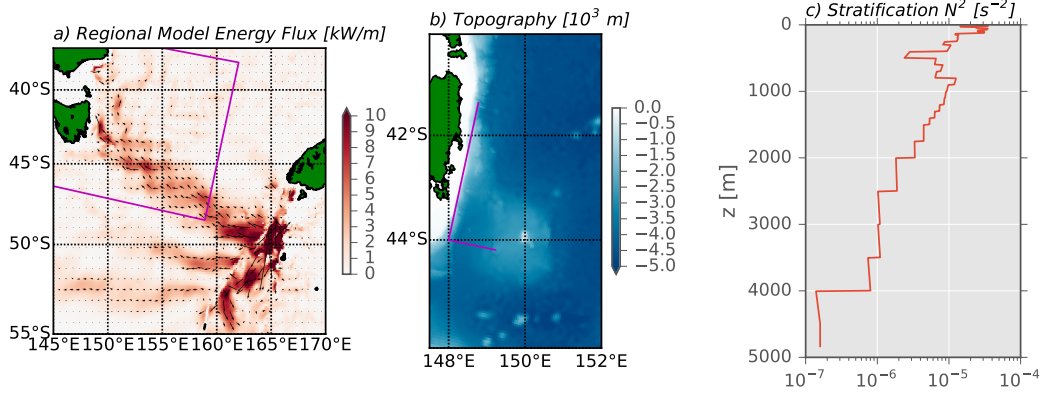


FIG. 1. Location of [TTide experiment TTIDE field site](#): a) Energy flux in a regional numerical simulation. Color is the absolute value of the flux, arrows its direction. The magenta box indicates the numerical modeling domain used in this paper. b) Detail of the bathymetry on the Tasman slope. The magenta lines indicate 100 km in the x-direction, and 300 km in the y direction in the modeling domain used in this paper. [c\) The stratification used for all runs in this paper, taken from the World Ocean Atlas at 152°E, 44°S \(Boyer et al. 2013\). The steps are due to linear interpolation of the density between the atlas depths.](#)

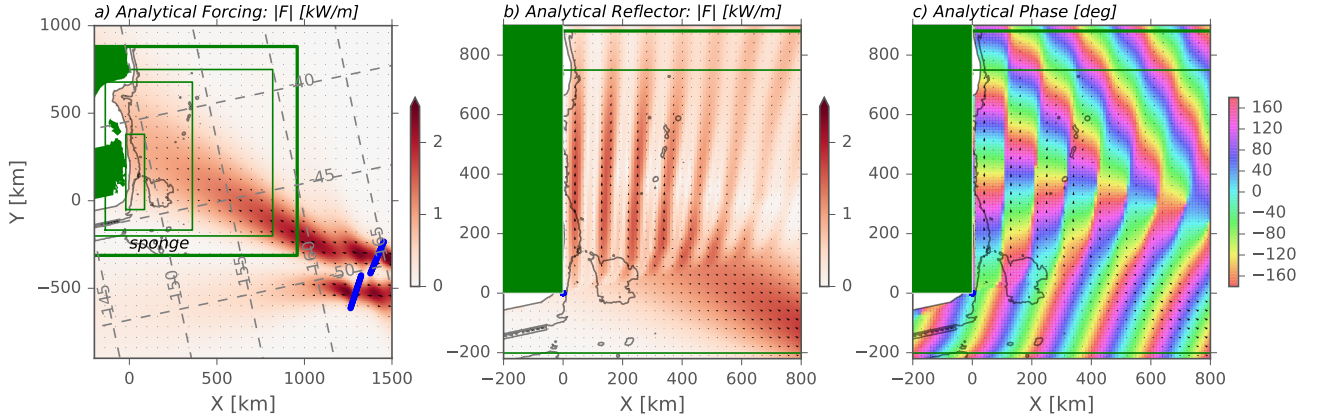


FIG. 2. a) Forcing Energy flux representation of the analytical response to the forcing used to drive the models used in this paper. Two mode-1 internal wave sources are located to the south east (blue lines). The model domain is rotated 12 degrees from geographic so the shelf break approximately lies along $x = 0$. Typical The outer model domain is the rectangle with the thick green line. The inner green rectangle denotes 1-km lateral resolution. Outside this rectangle resolution increases 3.5% per cell to a maximum of 5-km in the second largest rectangle, and outside this rectangle grid size increases to a maximum of 10 km. The sponge region layer is indicated as green rectangles by the largest thin-green rectangle. The 250, and 3000-m isobaths are contoured, though the bathymetry is not used in the analytical response. Arrows show the direction of the energy flux, and are scaled by its strength. b) Energy flux of analytical response of energy reflecting from a wall at $x = 0$, north of $y = 0$, in a flat-ocean domain. c) Phase of reflected response.

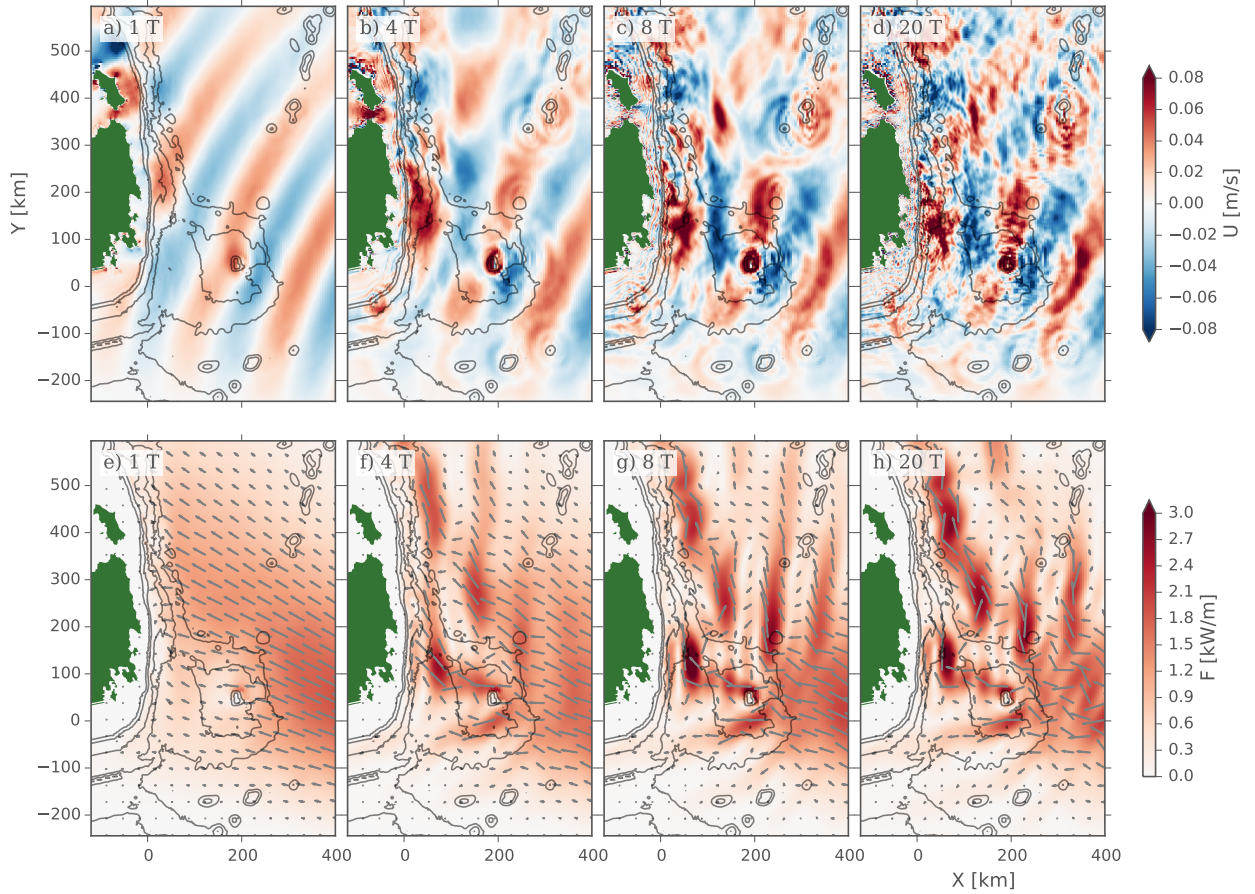


FIG. 3. a)–d) Surface x-direction velocity for four snapshots. a) is the initial conditions (slightly modified after a tidal cycle) and d) is the steady state. Grey contours are depths at 3000, 2000, 1000, and 250-m. e)–h) is depth-integrated baroclinic energy flux at the same time periods, with arrows indicating direction.

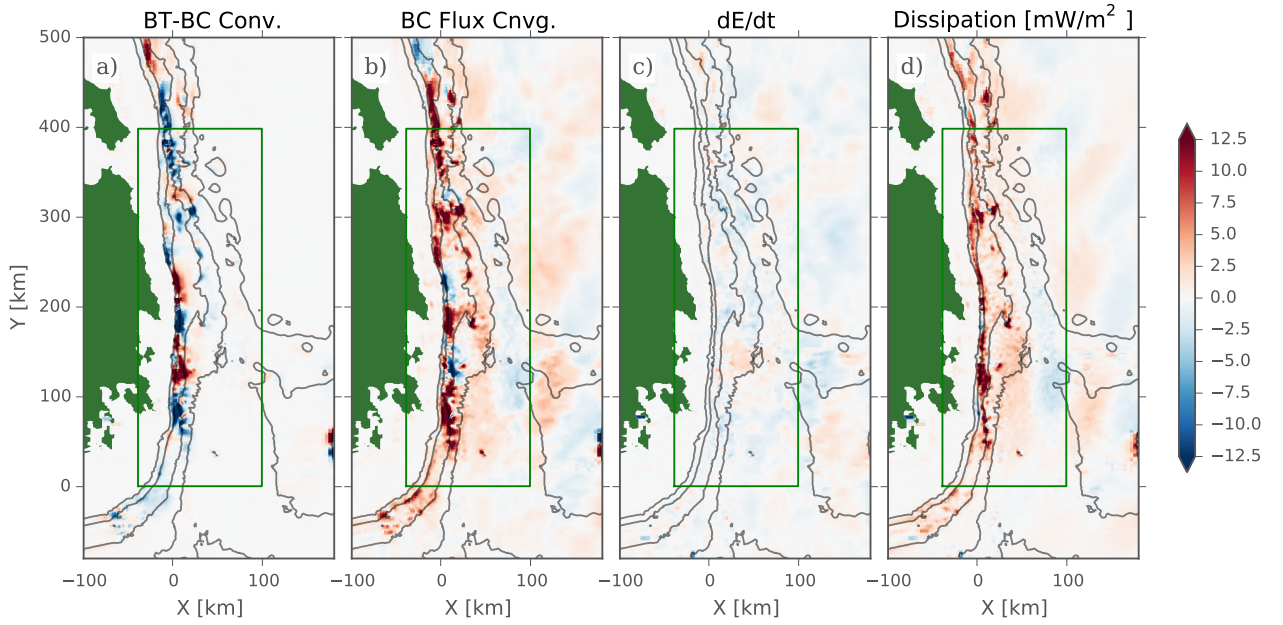


FIG. 4. Energy budget over the 19th tidal cycle of a) Barotropic to baroclinic conversion; b) Baroclinic energy flux convergence ($-\nabla F_{bc}$); c) rate of change of baroclinic energy; d) residual representing the dissipation in the model $D = -\nabla F_{bc} + \text{Conv.} - dE/dt$. The green box is the region for the energy time series (FIG. 5b).

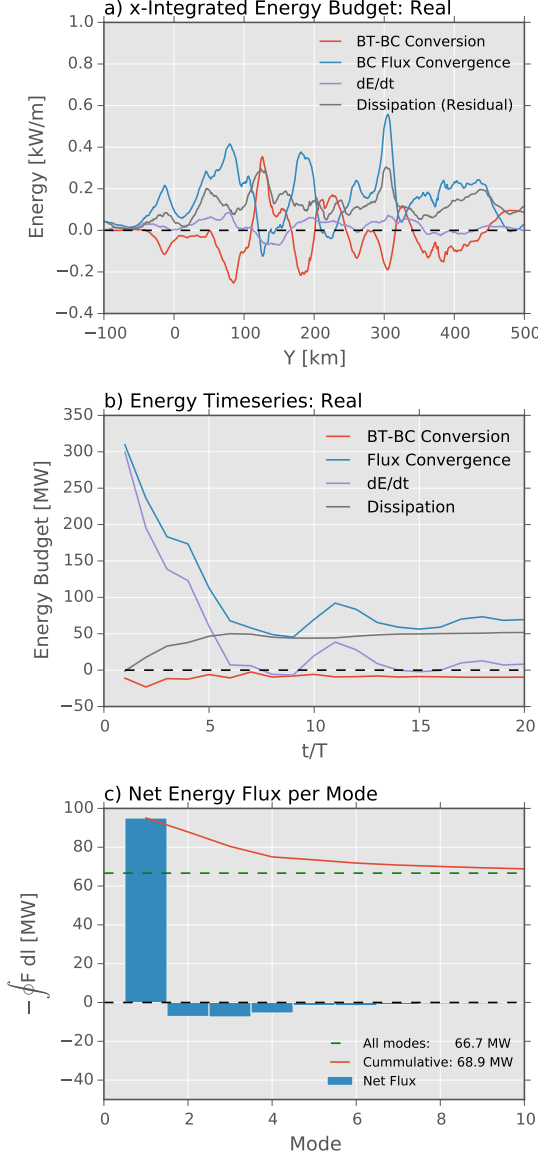


FIG. 5. a) Integral in x to 80 km offshore of the energy terms in FIG. 4 for the REAL case (averaged over 20th tidal cycle). Note that the barotropic-baroclinic term (red) is of the same order as the baroclinic convergence (cyanblue) and the residual dissipation (gray) for most of the slope. b) Energy budget time series for the “Real” case, tidally averaged, where time is normalized by $T = 12.4 \text{ h}$, between $y = 0$ to $y = 400$ km. There is still a small residual increase in the energy with time (purple), representing the accumulation of high-mode energy in the region. Net barotropic-baroclinic conversion (red) is small and negative, indicating a small net loss to the barotropic tide in this region. The bulk of the budget is the balance between baroclinic flux convergence (blue) and the residual “dissipation” (gray). c) Net flux (averaged over 20th tidal cycle) in the box defined by $0 < x < 80$ km, and $0 < y < 400$ km. Green is the value for the net flux (no modal decomposition). Blue bars are the modal decomposition. There is a net incoming flux in mode 1 and net reflecting fluxes in higher modes (primarily modes 2-4)₄₃

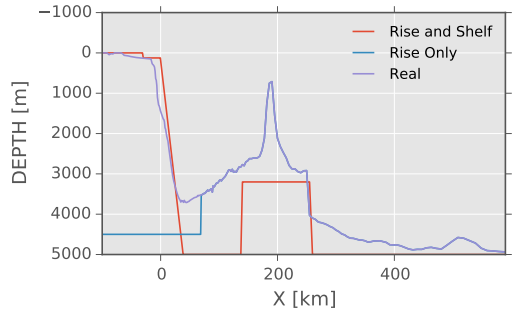


FIG. 6. Cross sections of topographies from $y = 50$ km.

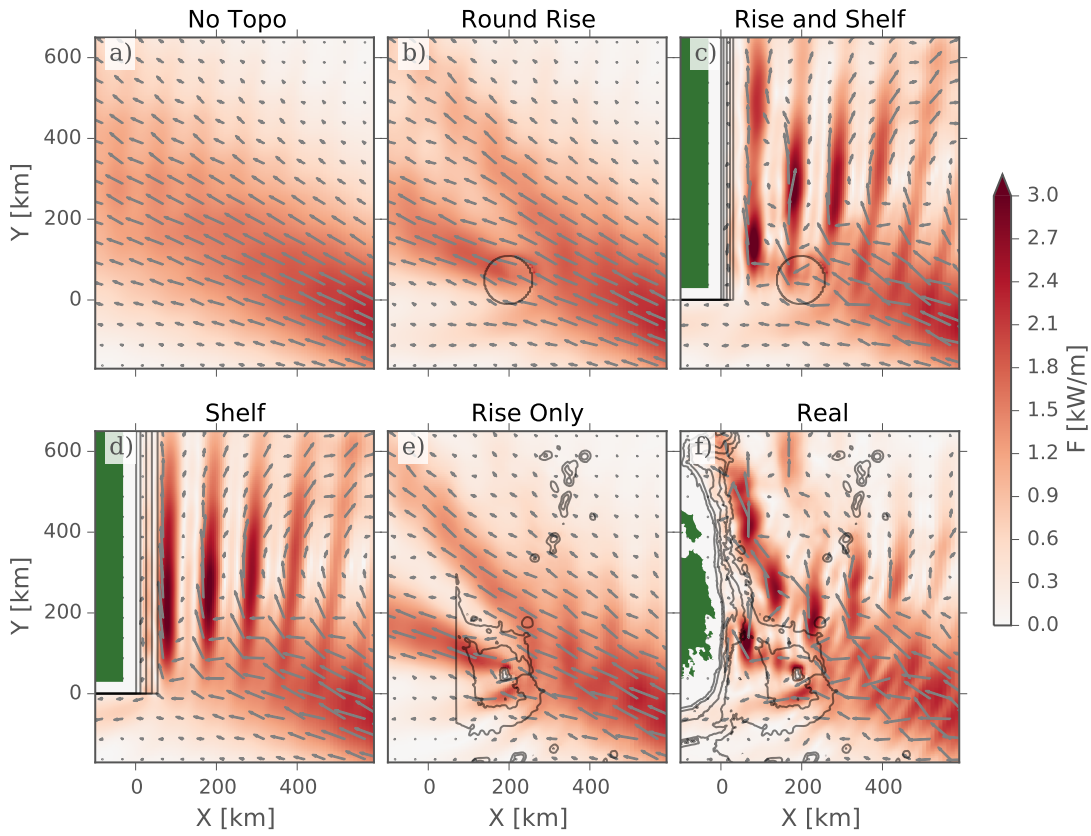


FIG. 7. Energy flux for six geometries at tidal cycle 20. Grey depth contours are -3000, -2000, -1000 and -250 m. Arrows indicate the direction of energy flux. See FIG. 6 for bathymetry cross sections at $y = 50$ km.

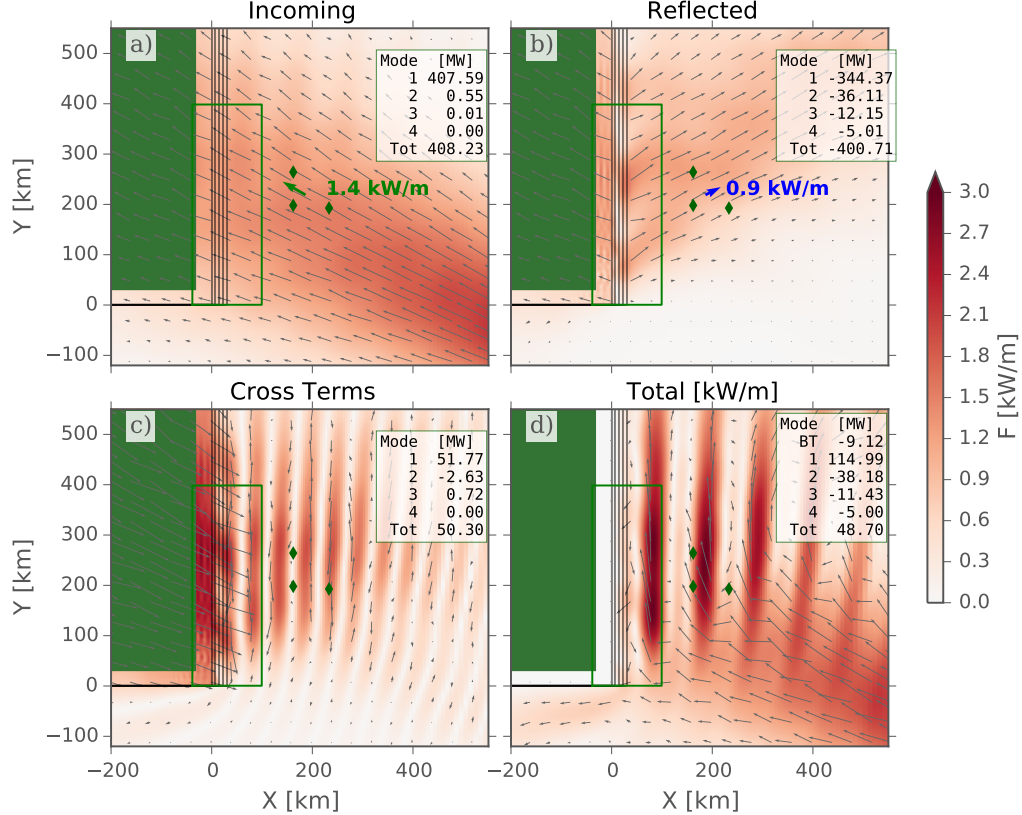


FIG. 8. Mode-1 decomposition of energy fluxes averaged for the 20th tidal cycle for the SHELF experiment. a) Incoming energy flux calculated from the NO TOPO simulation (FIG. 7a). Note that the shelf bathymetry is contoured on this plot (grey lines, and green “land”), but this bathymetry was not part of this simulation. The green line demarks the region the energy budget in the inset was integrated over. The green diamonds are the location of a synthetic mooring, and the arrow indicates the estimated incoming flux from a plane wave fit over the three moorings of the “Total” simulation (see text). b) Reflected energy flux calculated from the difference between the velocities and displacements of the Total simulation (panel d) and the “Incoming” (panel a). Blue arrow is the outgoing flux from a plane wave fit over the mooring array from the “Total” simulation. c) Energy flux cross terms between the incoming and outgoing waves. d) Total simulation from the SHELF case (FIG. 7d)

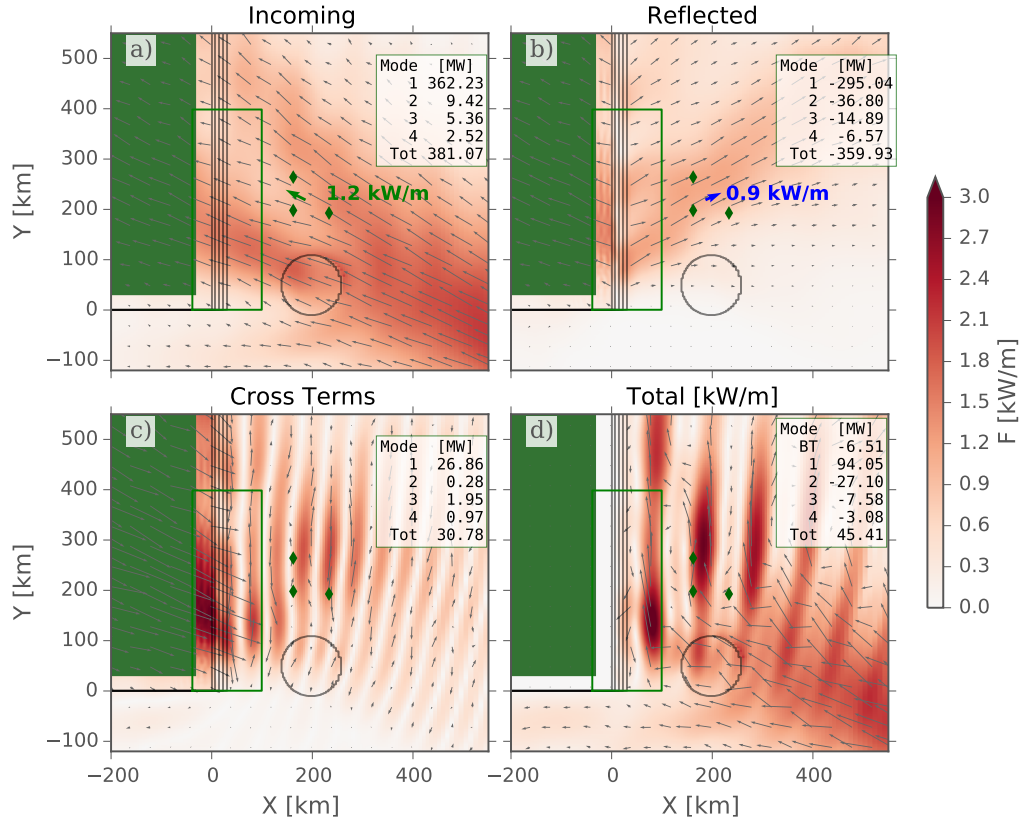


FIG. 9. Energy partition as in FIG. 8, taking the ROUND RISE simulation as the incoming wave, and SHELF/RIZE simulation as the total wavefield.

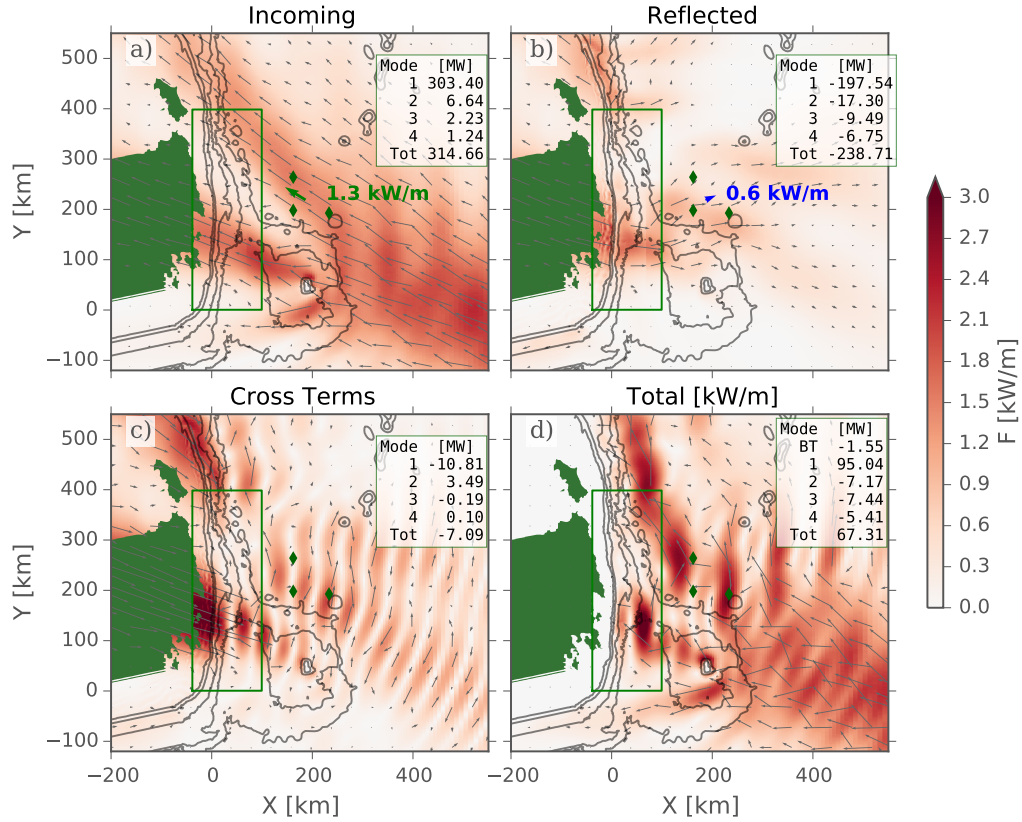


FIG. 10. Energy partition as in FIG. 8, taking the RISE simulation as the incoming wave, and REAL simulation as the total wavefield.

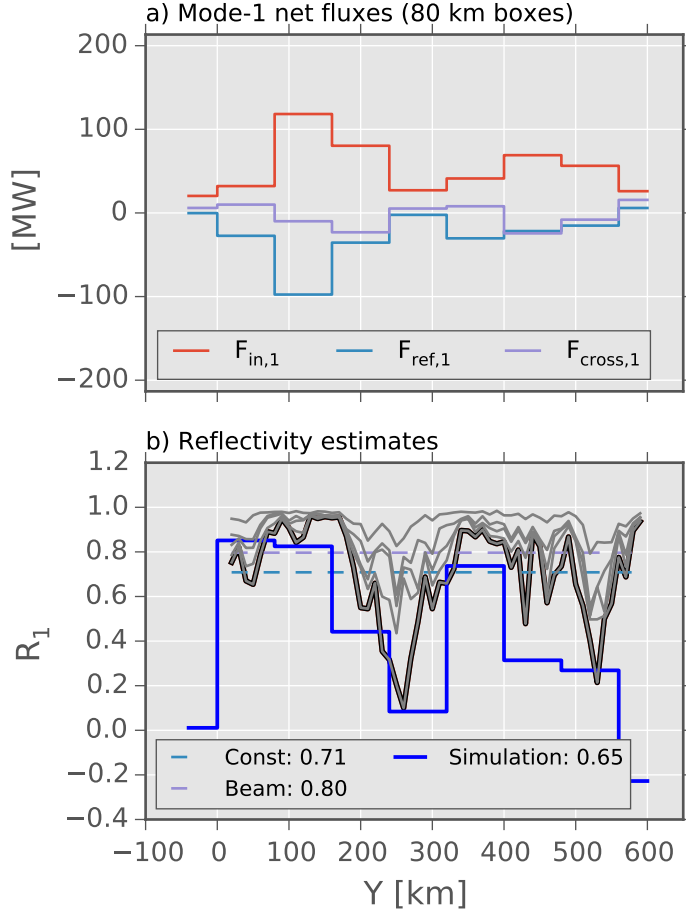


FIG. 11. a) Energy budget from 80 km by 80 km control volumes along the continental slope from the [20th tidal cycle of the](#) REAL simulations. The incoming flux (red) is compared to the reflected (blue) and the cross terms (purple). b) The reflection co-efficients. The blue line is R_1 , the mode-1 reflectivity in the 80-km control volumes along slope from the non-linear simulation. The black line is the mode-1 reflectivity from a linear model (Kelly et al. 2013a), ~~and~~ the [next four](#) grey lines ~~behind~~ are the cumulative sum of modes 2 ~~to~~ 5, and ~~then~~ the last grey line the sum of all the ~~modes~~ reflected energy. These do not sum up to one because the linear model has some “viscosity” that removes some high-mode energy. The dashed lines are the mean of R_1 from the linear model if a constant average is taken (light blue, dashed), and if weighted by the diffracted beam strength (purple, dashed).

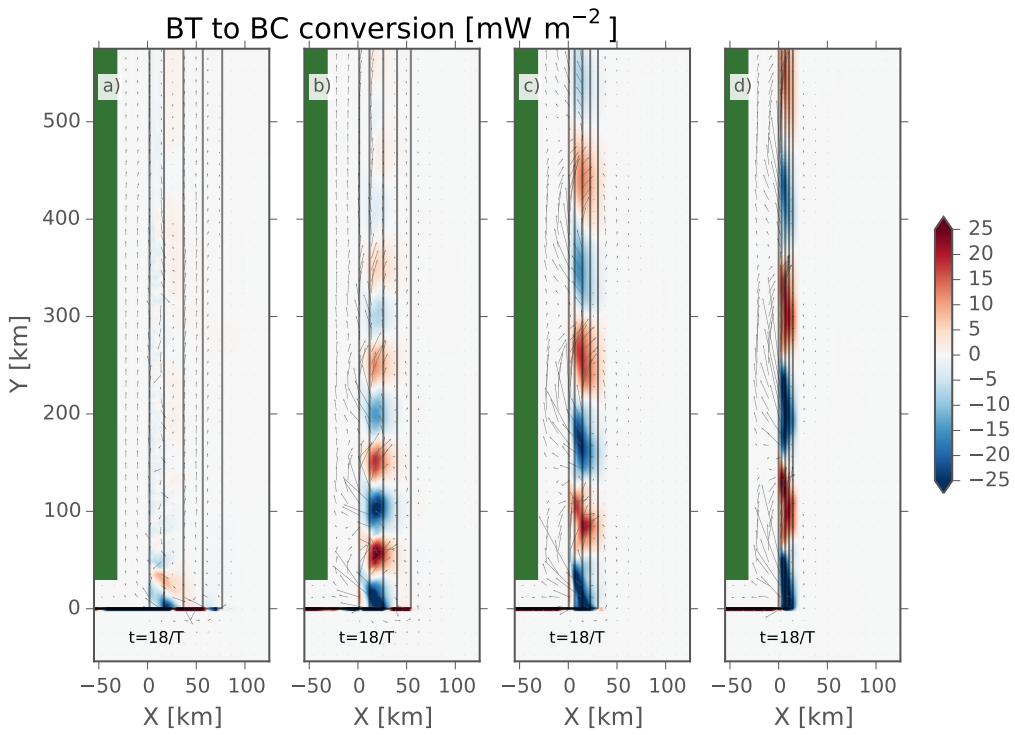


FIG. 12. Barotropic to baroclinic conversion averaged over the 18-th tidal period for different shelf widths from widest (a) to narrowest (100 km, b) 70 km, c) 40 km, and d) 20 km. Arrows are barotropic flux vectors. Note how the along-slope barotropic flux is almost entirely confined to conversion dipoles along slope.

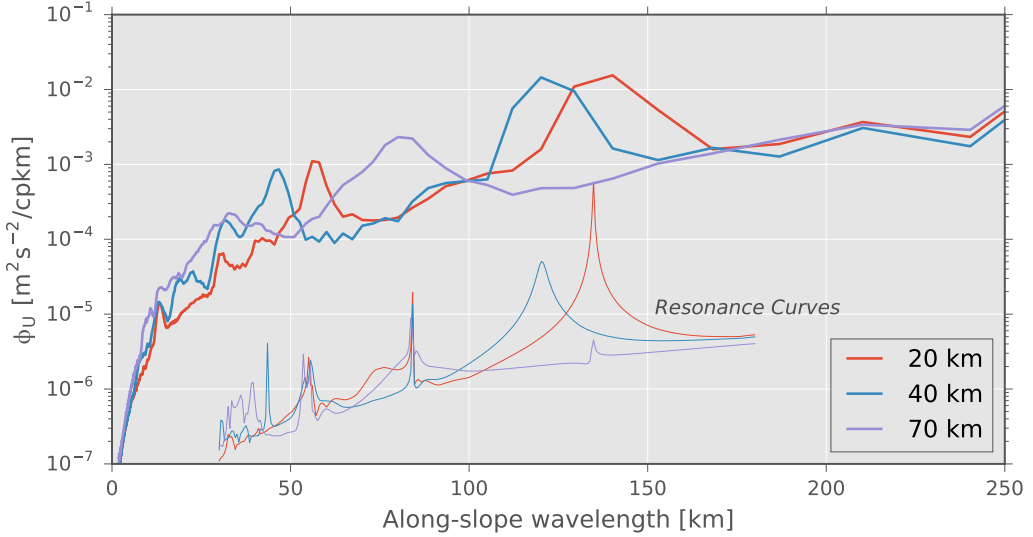


FIG. 13. Along-slope spectra of across slope velocity (thick lines) for the three narrowest slopes in FIG. 12, from velocities on the shallow shelf in these simulations. The thin lines are resonance curves, formed from the cross-slope equations of motion assuming harmonic motion in time and along-slope. As along-slope wavenumber is varied resonant modes have a stronger response. What is plotted is arbitrary units for the three slope geometries.

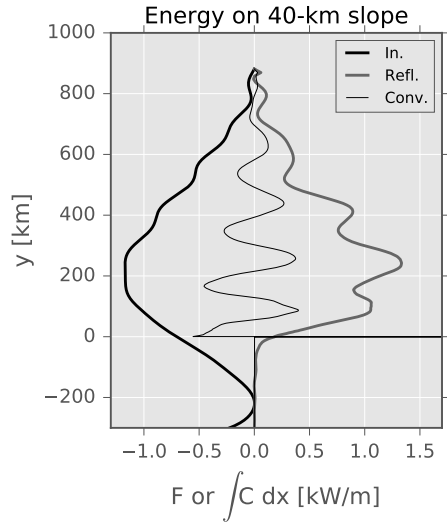


FIG. 14. Terms from the energy budget for 40-km wide slope. The incoming and reflected energy fluxes are computed at $x = 40$ km, and the conversion term integrated from the shelf to $x = 40$ km.

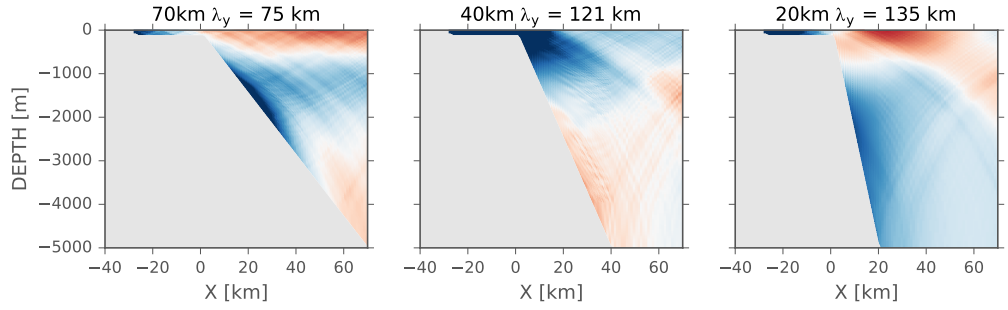


FIG. 15. Spatial shape of modes picked out from the resonant searching technique (as shown in FIG. 13) for the 70, 40 and 20-km wide slopes.